The Nature and Role of the Gold-Krypton Interactions in Small Neutral Gold Clusters

Luis A. Mancera*,† and David M. Benoit‡

Institute of Theoretical Chemistry, University of Ulm, Albert-Einstein-Allee 11, D-89069 Ulm, Germany, and The University of Hull, Cottingham Road, Kingston upon Hull HU6 7RX, UK

E-mail: luis.mancera@uni-ulm.de

Abstract

We investigate the nature and role of krypton embedding in small neutral gold clusters. For some of these clusters, we observe a particular site-dependent character of the Kr binding that does not completely follow the criterion of binding at low-coordinated sites, widely accepted for interaction of a noble gas with closed-shell metal systems such as metal surfaces. We aim at understanding the effect of low dimensionality and open-shell electronic structure of the odd-numbered clusters on the noble gas-metal cluster interaction. Firstly, we investigate the role of attractive and repulsive forces, and the frontier molecular orbitals. Secondly, we investigate the Au–Kr interaction in terms of reactivity and bonding character. We use a reactivity index derived from Fukui formalism, and criteria provided by the electron localization function (ELF), in order to classify the type of bonding. We carry out this study on the minimum energy structures of neutral gold clusters, as obtained using pseudo potential plane-wave density functional theory (DFT). A model is proposed that includes the effect of attractive electrostatic, Van der Waals and repulsive forces, together with effects originating from orbital overlap. This satisfactorily explains minimum configurations of the noble gas-gold cluster systems, the site preference of the noble gas atoms, and changes in electronic properties.

1 Introduction

Interaction of noble gases with metals is a common process in a wide set of experimental techniques and has been studied for systems such as metal surfaces (see Refs. 1–3 and references therein). Metal clusters and in particular small neutral gold clusters are interesting systems to gain an understanding of that interaction due to their particular geometries and asymmetric electrostatic potentials. In addition, due to the spin-polarized character of the odd-numbered gold clusters, they are also suitable for the study of the interaction between noble gas and metal in open-shell systems. Properties investigated in several studies of small gold clusters,[4–22] such as binding energy, ionization potential and electron affinity, show an alternating behavior between even- and odd-numbered structures. Hence, we might expect a manifestation of this alternating behavior on the noble gas-metal cluster interaction.

The largely accepted fact that noble gases adsorb at high-coordinated sites of metal surfaces has been superseded by the outcome of studies which show preferential adsorption at low-coordinated sites, as highlighted by Da Silva *et al.*[1] They investigate the Xe adsorption on metal surfaces from first-principles, and conclude that this effect is due to a site-dependent Pauli repulsion and polarization of the Xe adatoms and topmost substrate atoms. More recently, Da Silva and Stampfl[2] have studied the adsorption for a set of noble gases (He, Ne, Ar, Kr, Xe) interacting with a palladium surface and they obtained similar trends for He and Kr than those obtained for Xe. In particular, using LDA exchange-correlation functional, all these noble gases adsorb at top sites, while using PBE and PW91, the adsorption site preference changes for Ne and Ar to hollow-fcc sites. Müller[3] argues that chemical effects are not likely to play an essential role in the interaction of noble gases with metal surfaces, and that this interaction is instead driven by the overlap of the electrostatic atomic potentials of the interacting species.

Various experimental studies point out the important effects of noble gas embedding on the properties of the

gold atom and small gold clusters. Firstly, about 50 years ago there were already experimental evidences of the existence of bonds between metal complexes and noble gas atoms, even if they were recorded at the beginning as short-lived transients. Some representative experimental studies have been performed by Seidel and Seppelt[23,24] who investigated gold-xenon bonds in $AuXe_n^{2+}$ cationic compounds and claim that xenon functions as a σ donor towards Au^{2+} with a large charge transfer. A few theoretical studies[25–27] describe that bonding in terms of charge transfer from the noble gas to the metal atom or due to electrostatic interactions mainly. Secondly, matrix effects on metal clusters can be significant for heavy rare gas matrices, since even a weak interaction between a matrix support and a molecular metal cluster can strongly influence the electronic, vibrational and geometrical properties of such a cluster.[28,29] Thirdly, effects of noble gas atoms on infrared spectra of a number of small metal clusters in gas phase have been widely documented. Although Fielicke *et al.*[30] showed using far-infrared spectroscopy (FIR-MPD) that Ar embedding does not change significantly the geometry and electronic structure of neutral and cationic niobium clusters, Knickelbein and Menezes[31] observed that argon atoms bind with different efficiencies to each of the Nb_7, Nb_9 and Nb_{11} clusters, presumably due to a change in the nature of the binding. Gehrke *et al.*[32] observed significant changes in the FIR-MPD vibrational spectra of small Co_n^+ clusters as a function of the number of Ar atoms bound to the cluster. Fielicke *et al.* in another FIR-MPD study[33] observed variations of the experimental vibrational frequencies as a function of the number of argon atoms bound to the neutral silver trimer. More recently, Gruene *et al.* reported a FIR-MPD experimental study of neutral clusters (Au_7, Au_{19} and Au_{20})[34] in which krypton atoms are picked up by the clusters during their production and cause a larger effect on signal IR intensities than on vibrational frequencies. A very recent complementary study of the same group by Ghiringhelli *et al.*[35] including FIR-MPD spectra for Au_3 and Au_4, shows that these krypton atoms are not so loosely bound to the clusters, *i.e.* they localize at a defined adsorption site around these clusters and form a weak chemical bond.

Different models have been proposed to explain the interaction of noble gases with metal clusters. For example, Gehrke *et al.*[32] suggest an electrostatic picture of the interaction between argon and Co_n^+ clusters with a strongly repulsive short-range component arising from the Pauli repulsion, in which changes of the IR spectra are attributed to a mere polarization of the argon atoms. Jamshidi *et al.*[27] classify the bonding of noble gas atoms to metal clusters as partially electrostatic and partially covalent using the concept of 'atoms in molecules' (AIM) developed by Bader.[36,37] Ghiringhelli *et al.*[35] claim that a simple electrostatic picture is not enough for the interpretation of this type of bonding in small neutral gold clusters, which is in agreement with our main hypothesis in the present study.

Since an understanding of the interaction between noble gas atoms and small gold clusters is important to rationalize various experimental findings, we believe that is pertinent to investigate the nature of this bond in more detail and extend the analysis to its progression for clusters with different sizes and/or in dependence of the position at which the noble gas atoms bind the cluster. We decided to investigate the nature of this interaction using krypton as a probe, due to the fact that most recent FIR-MPD experiments[34,35] use krypton as a noble gas embedding. Firstly, we investigate the electrostatic potential, the spin density and the frontier molecular orbital wave functions for the clusters, in order to explore main interactions taking place. Secondly, we investigate the possible occurrence of a chemical bond between krypton atoms and gold clusters. In particular, we study the ability of the cluster to undergo a electrophilic or a nucleophilic attack, in terms of a reactivity index,[38] which is derived from the Fukui function formalism.[39–41] We also look at the nature of the interatomic interactions in terms of the electronic localization function ELF,[42–45] which is a topological and quantitative method to detect and classify a bond. Finally, as local and semi-local density functionals do not include long-range correlation effects, DFT is known to fail to describe Van der Waals (dispersion) forces,[46] so that description of weak bonds such as Kr–Au by DFT may differ from more accurate state-of-the-art quantum chemistry calculations. Consequently, we evaluate the effect of dispersion corrections on the Kr binding energies. Note that we have compared Kr binding energies calculated using PBE/GTH to ROMP2 results for AuKr and Au_7Kr elsewhere,[47] and showed that despite quantitative differences, DFT provides qualitative trends for the Kr–Au binding. For example, we showed that the Kr binding energy for the AuKr molecule calculated using PBE/GTH agrees favorably with ROMP2 results and experimental data (including anharmonicity corrections). In the same study we also showed evidence of the large BSSE in MP2. It is worth noting that using a plane wave basis set in DFT avoids basis set superposition errors (BSSE) that are significant in wave-function-based methods.

The rest of our paper is organized into five sections: In Sec. 2, we present the relevant computational details. In Sec. 3, we present an outline of methods used to study the Kr binding. Section 4 contains the results for the interaction of Kr with gold clusters without considering dispersion interactions. In Sec. 5, we highlight the trends of our results and also introduce additional results that include dispersion interactions in order to perform a comparison. Conclusions are presented in Sec. 6.

2 Computational details

We perform plane-wave DFT calculations using version 3.11.1 of the CPMD code.[48] We use the Perdew-Burke-

Ernzerhof PBE[49] functional with two kinds of pseudo potentials: Vanderbilt (VDB) pseudo potentials[50] with a plane-wave energy cutoff of 30 Ry (408 eV) for gold, and norm-conserving Goedecker (GTH) pseudo potentials[51–53] with a plane-wave energy cutoff of 100 Ry (1361 eV) for gold and krypton. In both cases, relativistic effects are included in the pseudo potentials. Only the $5d^{10}6s^1$ valence electrons for Au and the $4s^24p^6$ valence electrons for Kr are considered. Although relativistic effects are included in the pseudo potential, including spin-orbit effects and calculating Van der Wals (vdW) energy contributions explicitly is beyond the scope of the version of the CPMD code used in our study. While spin-orbit effects are not included in our calculations, we calculate dispersion corrections for the Kr binding in two alternative ways: i) Using the method proposed by Grimme *et al.* with the damping function proposed by Becke and Johnson, that sets the dispersion contribution to finite values at short ranges.[54,55] For that we use version 3.1 of the DFT-D3 package, which is an implementation of Grimme's method provided by his group.[56] ii) Using the method proposed by Tkatchenko and Scheffler.[57] For that we use its implementation in version 5.3.5 of the VASP code.[58] In all cases the dispersion corrections are obtained *a posteriori* on the cluster structures previously optimized using the CPMD code.

We use periodic boundary conditions and a cubic supercell of $(15\ \text{Å})^3$ to avoid interactions between neighboring clusters. The electronic density was checked to be small enough at the border of the cubic box in order to assure that neighbor images do not interact each other. In all delicate cases, the clusters were aligned along the diagonal of the cube to allow the largest separation between periodic cluster images, which means that the effective separation distance is ~ 26 Å instead of 15 Å. The convergence criteria for wave function and geometry optimizations are set to 10^{-7} a.u. (largest element of the gradient for the wave function) and 5×10^{-5} a.u. (largest element of the gradient for the ions), respectively. For Vanderbilt pseudo potentials, we set parameter DUAL to 6.0 (ratio between the wave function energy cutoff and the density cutoff) and GC-CUTOFF to 10^{-5} (density cutoff for calculation of the gradient correction), in order to guarantee a smooth convergence of the wave function optimization. Geometry optimization is carried out by means of the limited-memory BFGS (L-BFGS)[59] method. The local spin density approximation (LSD) version of the functional is used for all the spin-polarized cases. Harmonic frequencies are calculated using the finite differences of analytical first derivatives with a step length of 10^{-2} bohr. Anharmonic frequencies were calculated using PBE/VDB in a similar way to our previous studies.[47,60,61]

Kohn-Sham energies are calculated using a Davidson diagonalization scheme[62] for PBE/GTH, and Lanczos diagonalization[63] for PBE/VDB. Reactivity indices are calculated from partial charges obtained using PBE/VDB. These charges are derived from the calculated electrostatic potential by a least squares fit to the potential of an analytical partial charge model.[64] Due to the periodicity of the cell in the plane-wave DFT code, calculation of electrostatic charges is not trivial and better accuracy is obtained when the molecule is considered as an isolated system. Thus, we use the Hockney Poisson solver[65] for the calculation of the electrostatic properties. These calculations using GTH pseudo potentials become computationally more expensive due to high memory requirement. Therefore, the use of ultrasoft pseudo potentials for this purpose is advantageous.

Löwdin population analysis[66,67] is carried out with the GAMESS-US code[68] for Au_2, Au_2Kr and Au_2Kr_2, by means of Gaussian-type orbital DFT calculations using the PBE functional and the augSBKJC(1f) basis set. This basis set corresponds to the standard SBKJC basis set and effective core potential (ECP) including scalar relativistic corrections,[69] with an extra set of functions f (exponent=0.89),[70] augmented by a set of s and p diffuse functions (exponent=0.01).[71] The (spin-correct) Z-averaged second-order perturbation theory (ZAPT)[72,73] and spherical harmonic basis functions are used. Geometry optimizations are performed using analytic energy gradients with a gradient convergence tolerance of 10^{-5} hartree/bohr.

Cluster binding energies are calculated as the difference between the total energy of the cluster and the sum of the energies of the isolated atoms. Krypton binding energies to the cluster are calculated as the difference between the total energy of the Au_nKr_m cluster and the sum of the energies of the Au_nKr_{m-1} cluster and the isolated krypton atom. Dispersion interaction corrections for Kr binding are computed as the difference between the dispersion energy for the Au_nKr system and the dispersion energy for the bare Au_n cluster. Clusters are visualized using the Visual Molecular Dynamics (VMD) program.[74] The use of various codes is due to the fact that the various theoretical tools used in our study are not implemented in a single code. For example, van der Waals corrections are available in VASP and DFT-D3 but not in the version of the CPMD used.

3 Theoretical approach

3.1 Reactivity index

To rationalize the interactions between a gold cluster and the Kr atom, we can consider the concept of reactivity index derived from the Fukui function formalism.[39–41] Reactivity indices give us information about which atoms in a molecule have a larger tendency to either loose or accept an electron, *i.e.* which atoms in a molecule are more prone to undergo an electrophilic attack or a nucleophilic attack, respectively. In order to find the preferred binding sites for krypton, we calculate reactivity indices as suggested by Mendez and Gazquez,[38]

$$f_k^{+,nuc} = q_k(n+1) - q_k(n)$$
$$f_k^{-,elec} = q_k(n) - q_k(n-1). \quad (1)$$

Indices $f_k^{+,nuc}$ and $f_k^{-,elec}$ are measures of reactivity toward nucleophiles and electrophiles, respectively. These are defined for every atomic position k in the cluster. Here $q_k(n)$, $q_k(n-1)$ and $q_k(n+1)$ correspond to the electronic charge of atom k in the cluster before reacting, and after donating or accepting an electron, respectively, with n as the number of electrons of the original system before any reaction. These charges q_k (also called partial charges) are calculated at each atom of the cluster as described in Section 2 and keeping always the ground state geometry of the n electron system. The sum of all indices in the cluster correspond to the total change in the charge of the molecule, satisfying the sum rules $\sum_k f_k^{+,nuc} = \sum_k f_k^{-,elec} = -1$. It also implies that the electronic occupation varies by +1 in each case. Largest absolute values of the indices $f_k^{+,nuc}$ or $f_k^{-,elec}$ denote reactive positions either for an nucleophilic or for an electrophilic attack.

Since a Kr atom is a closed-shell system it will unlikely accept more electrons. Instead, it will donate charge to the cluster so that a nucleophilic attack on the cluster is promoted. This implies that the Kr atom behaves as a nucleophile (able to donate electronic charge) and the cluster behaves as an electrophile (able to accept electronic charge). Therefore we refer in the following only to the $f_k^{+,nuc}$ indices that correspond to a nucleophilic attack undergone by the cluster in presence of the Kr atom.

3.2 Electron localization function (ELF)

Although useful, the wave function alone does not always provide a reliable measure of what happens in the interatomic region. Instead, the electron localization function[42–45]

$$ELF = \frac{1}{1 + \left(\frac{D}{D_h}\right)^2} \quad (2)$$

can often provide a better description of the nature of the interatomic interaction and the character of the bonding, since it provides a deeper insight into the shell structure by using an orbital-independent measure of the electron localization, as has been highlighted in various studies.[75–77] ELF depends on the total electronic density ρ, its gradient $\nabla\rho$, and the kinetic energy density $\sum_{i=1}^{N} |\nabla\psi_i|^2$, rather than on the orbitals. This avoids the non-uniqueness problem that stems from unitary transformations of the canonical orbitals.[42]

$$D = \frac{1}{2}\sum_{i=1}^{N} |\nabla\psi_i|^2 - \frac{1}{8}\frac{|\nabla\rho|^2}{\rho},$$
$$D_h = \frac{3}{10}(3\pi^2)^{2/3}\rho^{5/3}, \quad (3)$$
$$\rho = \sum_{i=1}^{N} |\psi_i|^2.$$

Here ψ_i denotes the singly occupied one-electron (spin-) orbitals in a N-electron system, and D_h corresponds to an uniform electron gas with spin density equal to the local value of ρ.

ELF does not only provide a topological view of the bonding but also reveals the shell structure of atoms, and its magnitude offers a way to classify the bonding interaction. The function is normalized to the interval [0;1], and is large where the Pauli repulsion is small, *i.e.* where two electrons with antiparallel spin are paired in space. An ELF value of 1 corresponds to a perfect localization and 0.5 to an electron-gas-like pair probability. Ionic regions usually show core attractors with values larger than 0.5, but they can have very low ELF values close to the atomic centers if a pseudo potential is used. For the interatomic region, the closer ELF is to 1 the most covalent character the bond has, while values close or equal to 0.5 denote a metallic character of the bond. ELF values smaller than 0.5 denote regions with an overlap of electronic density that, even if low, can be interpreted in the context of AIM[36,37] as an indicator of a binding interaction, *i.e.* of a net attractive force keeping the atoms bound together. Classifying electrons in those regions can be delicate and care has to be taken with the interpretation of delocalization for values where $D > D_h$.[75,76] Values close to zero do not necessarily mean perfect delocalization, since ELF is a relative measure of the Pauli repulsion with respect to an electron gas of the same density.

3.3 Dispersion interactions

Dispersion interactions are the attractive part of the van der Waals (vdW) interactions, although dispersion and vdW are often used as synonyms. These kind of interactions are weak intermolecular forces arising from quantum-induced instantaneous polarization multipoles in molecules, so that they can act between molecules without permanent multipole moments. They can be explained as instantaneous electron correlations between induced dipole moments from one part to another part of a molecular system operating at a long-range scale.[78] Since dispersion is basically a local, atom-like property, theoretical schemes including a term $\propto r^{-6}$ tend to work well to describe this type of interaction, although it has been shown that a r^{-6} interaction can fail to describe some metallic low dimensional systems due to non-additive higher-order effects.[57,79] Contributions with r^{-8} and r^{-10} dependence

have also been used as part of some dispersion corrections in molecular systems.[80] Contributions of higher order such as r^{-12}, which is of a shorter range that r^{-6}, would already account for short- and medium-range dispersion.

It is known that all semi-local DFT functionals and conventional hybrid functionals cannot provide the correct $\propto r^{-6}$ dependence of the dispersion interaction, a failure that was originally noticed in studies of noble gas dimers.[46] Usual exchange-correlation functionals use solely the electron-density and occupied orbitals, thus they do not account for the long-range interactions in the weakly overlapping regime involving unoccupied orbitals. However, various dispersion-corrected DFT schemes have been developed in the last few years. A detailed review of these methods is presented by Grimme.[78] We focus here only on some of the most popular corrections, the semiclassical corrections DFT-D, which are based on an atom pairwise additive treatment of the dispersion energy. This consists of a general form of the dispersion energy which is simply added to the Kohn-Sham energy:

$$E_{disp} = -\sum_{AB}\sum_{a=6,8,10,...} s_n \frac{c_a^{AB}}{r_{AB}^a} f_{damp}(r_{AB}), \qquad (4)$$

where AB denotes a sum over all atom pairs in the system, c_a^{AB} ($a = 6, 8, 10...$) denote the dispersion coefficients for atom pair AB, s_n are global scaling factors and r_{AB} is the internuclear distance. f_{damp} are damping functions used to avoid near singularities for small r and double-counting effects of correlation at intermediates distances.

In this study we deal with two types of dispersion corrections that we report with the following notation: i) D3-BJ for the Grimme's correction with a damping function to finite values (Becke and Johnson) at short ranges,[54,55] and ii) TS for Tkatchenko-Scheffler correction.[57] The D3-BJ type of correction has an empirical nature since its parameters do not depend on the electronic structure, but are rather obtained by fitting to experimental c_6 coefficients and/or post-Hartree-Fock binding energy data. One drawback of these type of empirical correction is that it can lead to large overcorrections for short and medium ranges. The TS type of correction instead determines the c_6 coefficients from the mean-field ground-state electron density, so that they are expected to be more accurate that the empirical ones. For additional details about these dispersion corrections schemes we refer the reader to the cited papers. It is expected for the best corrected DFT methods to be relatively close to the wave function based CCSD(T) approach for typical vdW interactions. Remaining differences would probably steam from other DFT problems.

4 The nature of the gold-krypton interaction

Due to the fact that high-level electronic structure methods are needed to obtain an accurate description of the Au-Au interatomic interaction (Au-Au bonding), we are not going to focus on this interaction in our study. As we are interested mainly in the interaction of the cluster with Kr atoms, we focus on a systematical study of the Kr binding to the gold clusters using plane-wave DFT. For a better insight into the Au-Au bonding, we refer the reader to studies in which some small gold clusters, mainly Au_2 and Au_3, have been studied in detail using higher level *ab initio* methods, for example the study carried out by Geethalakshmi *et al.*[81] Here, we start by studying the AuKr system, and since we are interested to know the progression of this interaction as the cluster size increases, we also study a set of closed- and open-shell gold clusters in the range Au_2–Au_9. The results shown in this section do not include dispersion energy corrections. Those will be presented separately in Sec. 5 in order to analyze their effects.

4.1 AuKr

Figure 1 shows the ELF values obtained for AuKr using GTH pseudo potentials for gold and krypton. The minimum value of ELF is 0.06, at the center of the Au–Kr path. By examining the Laplacian of ELF (not shown here), we observe that there is still an analytical continuity of the function at the center of the Au–Kr path, which indicates an orbital overlap. The deformation of the function around the nuclei observed in the 2D plot at the right side of Fig. 1 suggests an induced polarization on the atoms that would be originated from charge transfer due to the orbital overlap.

The calculated binding energy -26.0 meV is close to the experimental value, -30 ± 2 meV.[82] The calculated harmonic and anharmonic frequencies for AuKr are 25 cm^{-1} and 21 cm^{-1}, respectively. This latter value is in close agreement with the experimental frequency, 23 ± 2 cm^{-1}.[83] Assessing the PBE/GTH method by comparing it to ROMP2 shows that both BSSE-corrected ROMP2/def2-QZVPP and PBE/GTH provide a good description of the AuKr interaction.[47] The vibrational frequency is well reproduced, with ROMP2 providing a slightly higher anharmonic frequency (22 cm^{-1}) than PBE/GTH (21 cm^{-1}). The predicted interaction energies are either side of the measured value, with BSSE-corrected ROMP2/def2-QZVPP leading to a stronger interaction (-34 meV). Note that Plowright *et al.*[83] have calculated the binding energy as -36 meV at the RCCSD(T) level of theory, which exceeds $\sim$ 6 meV the experimental value. Nevertheless, their calculations are not BSSE corrected.

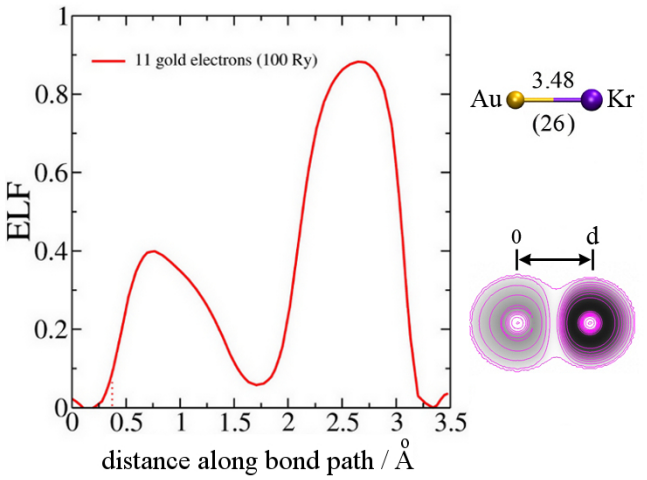

Figure 1: Electron localization function ELF for AuKr. Coordinate x is oriented along the bond with $x = d$ as the bond length. Vertical line indicate the limit of the core for the pseudo potential for gold. AuKr complex at the right part of the figure indicating the Au–Kr distance and the Kr binding energy (in parenthesis) in Å and meV/atom, respectively. 2D plot of ELF is color-coded from zero (white) to one (black) with isocurves in 0.1 steps. The lowest isocurve is set to 0.01, the others are exact multiples of 0.1. Results obtained using PBE/GTH.

4.2 Au_2Kr and Au_2Kr_2

A FIR-MPD experiment for Au_2 has not been yet reported. The difficulties to obtain the vibrational spectrum of Au_2Kr or Au_2Kr_2 with this technique are related, as declared by Ghiringhelli *et al.*,[35] to the higher ionization potential of the cluster in comparison to the energy of the ionizing laser used in the experiment. Classical experiments on Au_2 report the use of noble gases different to krypton (Ruamps[84] used argon, and Simard[85] and Bishea[86] used helium). The accepted reference value of the fundamental vibrational frequency of Au_2 (190.1 cm^{-1}) has been taken from the value reported by Ruamps. It should be remarked that for those classical experiments, an interaction of the noble gas atoms with the clusters during the measure of the vibrational spectrum is excluded, while for the FIR-MPD technique such an interaction is supposed to occur.

For Au_2, we obtain a bond length of 2.54 Å and a binding energy of -1.11 eV/atom, at the PBE/GTH level of theory. We investigate the effect of binding one and two krypton atoms to Au_2 in the configurations described in Fig. 2. Due to the symmetry, the Fukui reactivity indices have the same magnitude (-0.5) for each site. Krypton binding at the ends of the cluster yields a large deformation of ELF, indicating a strong polarization of Kr. Maximum ELF values at the center of the Au–Au and Au–Kr paths of Au_2Kr_2 are 0.33 and 0.11, respectively. This means that ELF changes from 0.29 to 0.33 at the center of the Au–Au distance by binding two krypton atoms, *i.e.* it becomes closer to but still far away from a metallic behavior (ELF=0.5). An ELF value of 0.11 at the center of the Au–Kr distance in Au_2Kr_2 indicates a larger orbital overlap and consequently a larger charge transfer from krypton to gold in comparison with the AuKr system which has ELF=0.06.

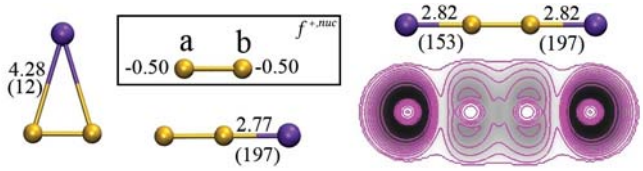

Figure 2: (**Left**) Bare Au_2 cluster in a box indicating the $f^{+,nuc}$ reactivity indices. Various possible configurations of the Au_2Kr_n clusters indicating the Au–Kr distance and the Kr binding energy (in parenthesis) in Å and meV/atom, respectively. For the perpendicular position the value of the distance is referred to the center of Au_2. (**Right**) 2D plot of the electron localization function ELF for Au_2Kr_2. The plot is color-coded from zero (white) to one (black) with isocurves in 0.1 steps. The lowest isocurve is set to 0.01, the others are exact multiples of 0.1. All results obtained using PBE/GTH.

By comparing Au_2Kr and Au_2Kr_2 in Fig. 2 with the electrostatic potential in Fig. 3, we observe a close agreement between the shape of the electrostatic potential and the orientation of the krypton atom for the minimum energy configuration. Krypton atoms behave as a polarisable electron cloud with a preference for binding at positions of metal clusters that exhibit a stronger positive electrostatic potential. In our case, this will be either ends of the gold dimer. The Kohn-Sham frontier orbitals for Au_2 shown in Fig. 3 reveal σ-type bonding characterized by a very slight deformation of the HOMO (d_{z^2}–d_{z^2} interaction) and the LUMO in the interatomic region. Interestingly, an analysis of the frontier molecular orbitals reveal that the HOMO is anti-bonding (σ^* character) due to a full set of d orbitals on each Au atom, indicating that the bonding in Au_2 is due to the favourable interaction of 6*s* orbitals on each Au center (third-highest occupied level) and above it, one has the 5d-based π^* and $\sigma*$ levels.

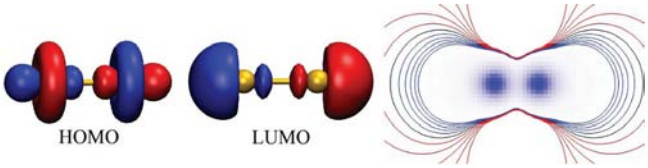

Figure 3: (**Left**) HOMO and LUMO for Au_2, using PBE/GTH. 0.05 $bohr^{-3/2}$ isosurface. (**Right**) 2D electrostatic potential for Au_2 with isocurves each 20 meV, using PBE/VDB. Blue and red isocurves indicate positive and negative potentials, respectively. Black line indicates zero potential.

Although the attractive electrostatic potential and the frontier molecular orbitals provide a satisfactory explanation for the Kr binding at the ends, a more complete picture of the Au–Kr interaction should include other contributions such as Pauli repulsion and Van der Waals (vdW) forces. For instance, the large distance of the krypton atom above the cluster indicates a typical Van der Waals-type interaction. In this case, the Au–Kr distance (4.45 Å) exceeds the sum of the Van der Waals radii[87] for gold (1.66 Å) and krypton (2.02 Å). The role of vdW interactions is expected to become predominant in the direction perpendicular to the cluster in which

there is a negative electrostatic potential. On the other hand, Pauli repulsion associated to the electronic density is expected not to affect significantly the site preference dictated by the electrostatic potential in the case of closed-shell clusters, but is expected to have more significance for the odd-numbered structures, due to the effect of the unpaired electron.

In order to investigate further the effects due to orbital overlap, we calculate the dipole moment and Löwdin populations[66,67] for the Au_2, Au_2Kr and Au_2Kr_2 clusters, using PBE/augSBKJC($1f$) and the GAMESS code.[68] Contrary to the bare Au_2 cluster which has a zero dipole moment, binding of a single krypton atom generates a dipole moment of 1.54 Debye for the complete system (Ghiringhelli *et al.*,[35] report 2.2 Debye). Population analysis reveals a charge transfer of $0.21e$ from Kr to the gold cluster, most of which ($0.17e$) is retained by the gold atom bound to Kr. Due to symmetry reasons, binding a second Kr atom restores the total dipole moment to zero but a charge transfer of $0.20e$ for each bond is observed. Since IR intensities reflect a change of dipole moment during vibration, an enhancement of the IR intensities might be expected by binding one (or more) krypton atom(s) to Au_2.

For the bare Au_2 cluster, we obtained a harmonic frequency of 176.2 cm^{-1} and an anharmonic frequency of 175.3 cm^{-1} using PBE/VDB. These values are $\sim$ 8% lower than the experimental frequencies, 190.9 cm^{-1} and 190.1 cm^{-1}, respectively. Nevertheless, the calculated anharmonic frequency is 0.9 cm^{-1} lower than the calculated harmonic frequency, keeping almost the same difference as the experimental values. We did not calculate anharmonic frequencies for the Au_2 cluster bound to a single Kr atom. In this case, the effect of anharmonicity is expected to be comparable to that observed for the bare cluster, since the noble gas atoms do not change the bond length of the gold dimer significantly. Two Kr atoms distort the geometry of the cluster decreasing its Au–Au length (2.538 Å) by only 0.005 Å. Despite this small change in bond length, the harmonic vibrational frequency is significantly affected. Using PBE/GTH, the harmonic frequencies for Au_2 and for the highest normal mode of Au_2Kr and Au_2Kr_2 are 172.2 cm^{-1}, 180.3 cm^{-1} and 185.2 cm^{-1}, respectively. *i.e.* One and two krypton atoms lead to an increase of the harmonic frequency by 8 cm^{-1} and 13 cm^{-1}, respectively. Compared to the noble gas effect, the vibrational anharmonicity of the Au_2 stretch fundamental (0.9 cm^{-1}) is almost negligible. An eventual FIR-MPD vibrational spectrum of Au_2Kr might show a fundamental frequency close to 200 cm^{-1}, *i.e.* 8 cm^{-1} above the value accepted from the experiment of Ruamps.[84] This would also be consistent with the value reported by Ghiringhelli *et al.*,[35] of 200 cm^{-1} using CCSD(T). A recent study of the bare gold dimer by Geethalakshmi *et al.*[81] using high level *ab initio* methods shows a value for the vibrational frequency of the ground state that is in very good agreement with the experimental value reported by Ruamps.

4.3 Au_3Kr, Au_3Kr_2 and Au_3Kr_3

DFT and *ab initio* methods show a potential energy surface (PES) for Au_3 including three structures very close in energy, in which Jahn-Teller and spin-orbit coupling effects play an important role.[88,89] Those structures are an obtuse triangle and a two acute triangles. Au–Au binding energy for the global minimum energy structure (obtuse triangle) of the bare Au_3 cluster using PBE/GTH is -1.18 eV/atom. The fact that the vibrational spectrum obtained in the FIR-MPD experiment agrees well with the theoretical spectrum of the acute structure, although obtuse and acute structures are very close in energy, has been explained by Ghiringhelli *et al.*[35] in terms of the vertical ionization potential, since the acute structure is presumably easier to be ionized than the obtuse one. Previous experiments show dissimilar results about the minimum energy structure for the neutral Au_3 cluster.[90–92]

Krypton embedding affects strongly the gold trimer, modifying the DFT global minimum energy structure (obtuse triangle), *i.e.* by binding krypton atoms, the acute structures become more stable than the obtuse one. Binding one krypton atom at the center of the obtuse triangle structure (see Fig. 4) does not change the angle of this cluster (136.5°). Binding one or two krypton atoms at the ends leads to a stronger bond than if one Kr atom is bound at the center, in agreement with the prediction given by the reactivity indices. In addition, this reduces the angle to 134.7° and 133.8°, respectively. On the other hand, by binding one krypton atom to the acute structure (with 65.8°) at site (b), the resulting acute triangle structure has an angle of 63.7°. Binding an additional krypton atom changes the angle to 55.8°. A third atom does not distort the structure further.

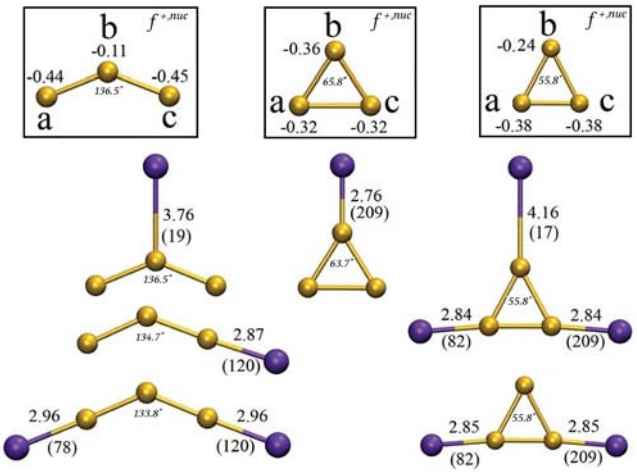

Figure 4: Bare Au_3 clusters in boxes indicating the $f^{+,nuc}$ reactivity indices. Various possible configurations of Au_3Kr_n clusters indicating the Au–Kr distance and the Kr binding energy (in parenthesis) in Å and meV/atom, respectively. The minimum energy for the bare cluster is the obtuse triangle, while the minimum energy for Au_3Kr_n clusters is the acute triangle. All results obtained using PBE/GTH.

Figure 5 shows the frontier molecular orbitals and electrostatic potentials for three isomers of Au_3. For all

cases, Kr binding follows the orientation of the electrostatic potential, whose positive regions are strongly related to the extended σ-type orbitals of the α-LUMO and β-LUMO. The energies for binding one krypton atom to the preferred sites of the obtuse and acute triangle structures are -120 meV and -209 meV, respectively, but the Au–Kr distances are quite similar, 2.87 Å and 2.76 Å respectively. It indicates that the attractive electrostatic potential favors a stronger Au–Kr bond for the acute structure, and that the strength of the interaction may be determined by the extension of these LUMOs. The spin density of the bare cluster, which follows the shape of the singly occupied molecular orbital β-SOMO and is related to the Pauli repulsion, would contribute to modify the electronic distribution after Kr bonding.

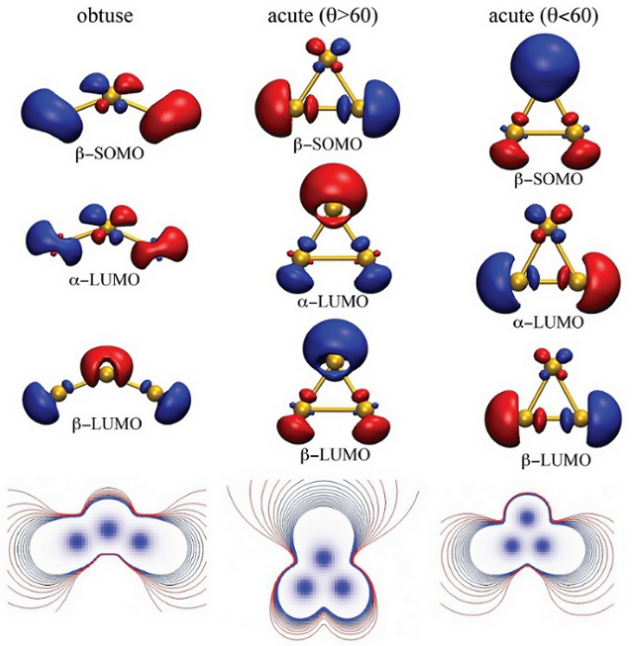

Figure 5: (**Above**) β-SOMO, α-LUMO and β-LUMO for Au_3, using PBE/GTH. 0.05 bohr$^{-3/2}$ isosurface. (**Below**) 2D electrostatic potential for Au_3 with isocurves each 20 meV, using PBE/VDB. Blue and red isocurves indicate positive and negative potentials, respectively. Black line indicates zero potential.

The main effect of the Kr embedding on Au_3 is that binding one krypton atom changes the global minimum energy structure from the obtuse to the acute triangle, thus modifying significantly the scenario of the vibrations. Harmonic frequencies 176.0/124.3/22.5 cm^{-1} for the obtuse triangle structure of the bare cluster using PBE/GTH become in the case of the acute structures 167.3/98.7/84.5 cm^{-1} for Au_3Kr, 176.1/107.7/77.3 cm^{-1} for Au_3Kr_2, and 176.3/107.6/77.5 cm^{-1} for Au_3Kr_3. This change from obtuse to acute structure affects mainly the harmonic frequency of the bending mode which changes by more than 50 cm^{-1}.

4.4 Au_nKr $(4 \leq n \leq 9)$

Fig. 6 shows the minimum energy structures (enclosed in boxes) for the bare Au_n clusters with $4 \leq n \leq 9$ indicating the $f^{+,nuc}$ reactivity indices. The Au–Au binding energy for those structures are -1.48, -1.62, -1.84, $-1.xx$, $-1.xx$, and $-1.xx$ eV/atom, respectively as obtained using PBE/GTH. The same figure also shows different configurations for the Au_nKr clusters. In general, larger strengths of the Au–Kr interaction are associated with shorter Au–Kr distances.

Krypton embedding distorts largely the Au_4 cluster but without modifying its minimum energy structure. The large deformation of the geometry leads to an increase of the harmonic frequency of the largest normal vibrational mode by $\sim$3 cm^{-1}. The magnitude of the binding is almost six times stronger for binding at (a) than for binding at (b), -150 meV/atom against -24 meV/atom. The reactivity indices are in agreement with this site preference. Note that Kr binds preferably the atom which has three first neighbors, *i.e.* at (a) or (c), instead of the ones which have only two first neighbors at (b) or (d). It is clear that binding at a low-coordination site does not apply for this closed-shell cluster. For Au_5, Kr adsorbs preferentially at site (b) in agreement with the site preference given by the reactivity indices. The deformation of this and larger clusters due to the effect of Kr embedding is rather than small if it is compared to Au_4. The preferred positions of krypton to bind the Au_6 cluster are the corners, which also have the lowest coordination, in agreement with the reactivity indices. For Au_7, the possible positions at which the krypton atom binds are clock-wise denoted from (a) to (g) although at position (g) krypton binding is not favored. The position above the plane is denoted as (top). The site preference of Kr to attach the cluster evidences the preference of the noble gas atom to bind at a low-coordinated site, in this case at (a). Nevertheless, the order of the binding energy dictated by the coordination number is not followed for configuration (e) which has coordination three but is preferred over positions (c) and (f) which have coordination two. Contrary to the previous clusters, for Au_7 the site preference does not follow the reactivity indices. For Au_8, the preferred sites of Kr to bind the cluster are the corners, which have the lowest coordination and the larger reactivity indices. For Au_9, Kr also prefers to bind the cluster at corner sites. The reactivity indices show a binding preference of the Kr atom for site (f) which has coordination three, followed by sites (a) and (c) which have coordination two. Since the Kr atom binds preferentially at site (a), the site preference does not follow completely the reactivity indices for this cluster. In summary, preferential Kr binding to the corners is observed for the different clusters. Nevertheless, exceptions to binding at low coordination sites are observed for Au_4 and Au_7, and exceptions to the reactivity indices are observed for Au_7 and Au_9.

A better understanding of the Kr binding site preferences is obtained by looking at the electrostatic potential and the frontier molecular orbitals shown in Fig. 7. In general, for all cluster sizes the most favorable position to bind a krypton atom coincides with the position

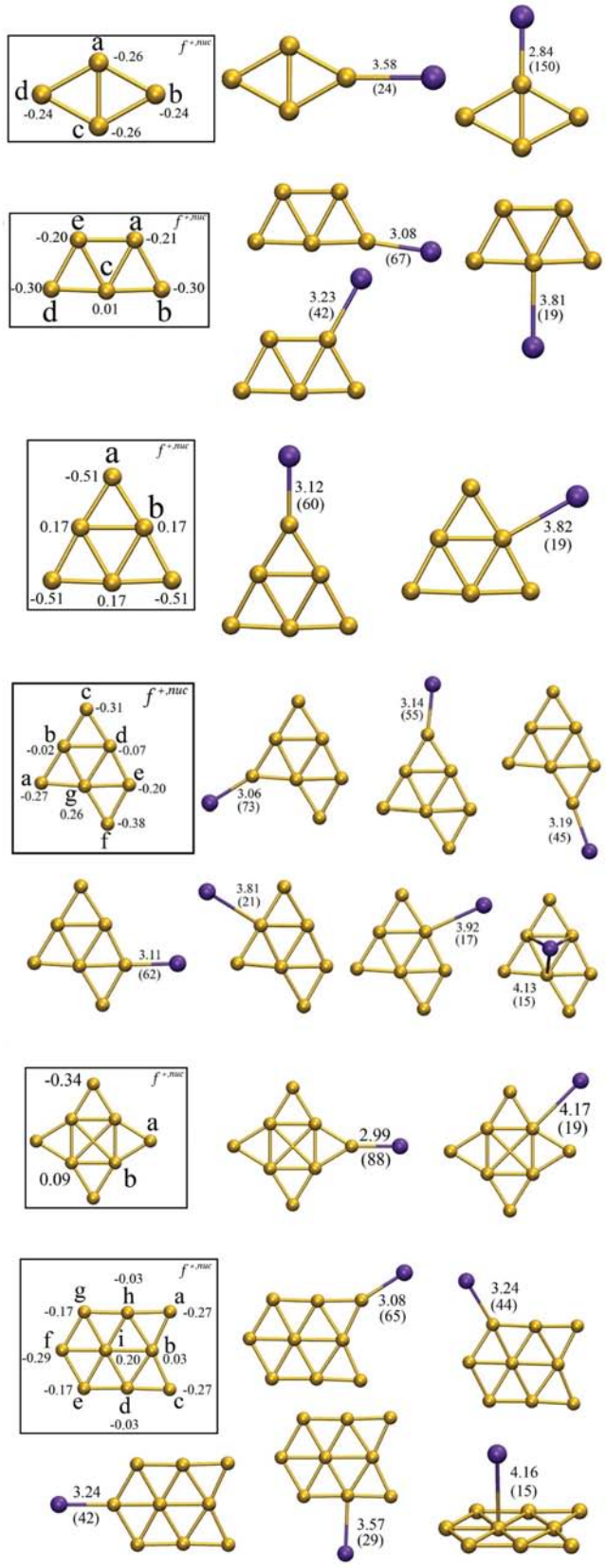

Figure 6: Bare Au_4-Au_9 clusters in boxes indicating the $f^{+,nuc}$ reactivity indices. Various possible configurations of Au_4Kr-Au_9Kr complexes indicating the Au–Kr distance and the Kr binding energy (in parenthesis) in Å and meV/atom, respectively. All results obtained using PBE/GTH.

where the electrostatic potential is the most positive, *i.e.* at the corners, so that the site preference and orientation of the krypton atom is mainly governed by the distribution of the electrostatic potential. Atomic positions in the plane of the cluster different to the corners are characterized by negative partial charges that lead to a more negative electrostatic potential around. Positions above/below of the cluster are also characterized by a negative electrostatic potential.

On the other hand, the frontier molecular orbitals provide an alternative way to analyze the Kr binding site preference. For all clusters structures the site preference is closely related to the more extended σ-type orbitals of the LUMO, which occurs at the corners. Nevertheless, for the open-shell structures Au_5, Au_7, and Au_9 is observed that the spin density, which follows the shape of the β-SOMO and can be a descriptor of the Pauli repulsion, can modulate the effect of the LUMO. For example, for Au_5 β-SOMO is more extended at positions (a), (c) and (e) leading to a magnitude of the binding energy at (c) only three times smaller than at position (b) although a vdW-type bond is favored at (c). For Au_7, the preference for binding at site (a) is mainly explained by the larger extension of the electrostatic potential around (a), enhanced by a favorable lower Pauli repulsion originated from a low spin density around this corner (see β-SOMO in Fig. 7). The larger deformation of the cluster when the binding occurs at sites (a) or (e) is explained as a consequence of a stronger Kr–Au interaction at these sites product of a significant orbital overlap at the β-LUMO. The preference of binding at site (e) over sites (c) or (f), which have lower coordination number, is also explained by the large orbital overlap, which at site (e) is contributed from the large extension of the σ-type orbitals of both α-LUMO and β-LUMO. The role of the vdW interactions become predominant as the electrostatic potential becomes negative. This is the case of the direction perpendicular to the cluster (top) and positions (b) and (d). For Au_9 we observe that, although the electrostatic potential is less negative around (g) than around (f), binding at these sites show similar values for energy and bond length. This is probably due to the combined effect of the frontier orbitals at these positions. For example, the effect of a larger α-LUMO at (f) might be counteracted by a larger Pauli repulsion due to β-SOMO. For binding at position (d), the relative large extension of the σ-type orbitals of the β-LUMO keeps the krypton atom relatively close to the cluster, in comparison with the situation in which it is above the cluster.

To rationalize the role of the van der Waals interactions we analyze the ELF in a few selected cases. This allows us to visualize some differences between Kr binding at corner sites and at high-coordinated sizes. For example, for Au_4 the analysis of ELF in the Au–Kr interatomic regions show values 0.12 and 0.06 for binding at positions (a) and (b), respectively. This suggests that the Pauli repulsion at the center of the bond at (a) is twice the repulsion at the center of the bond at (b). Binding at

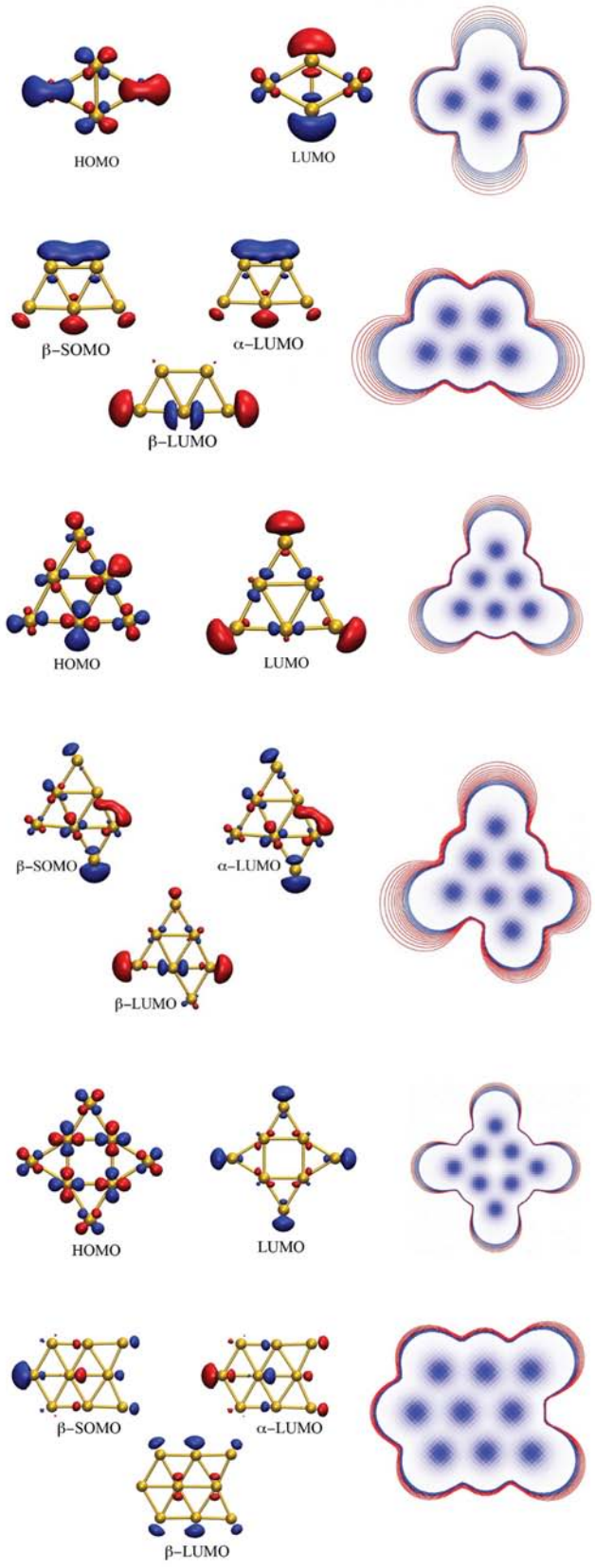

Figure 7: (**Left**) Frontier molecular orbitals for Au_4-Au_9 clusters, using PBE/GTH. 0.05 bohr$^{-3/2}$ isosurface. (**Right**) 2D electrostatic potential with isocurves each 20 meV, using PBE/VDB. Blue and red isocurves indicate positive and negative potentials, respectively. Black line indicates zero potential.

site (b) occurs within a typical vdW regime, as is also expected for regions out of the plane, where the electrostatic potential is negative. Figure 8 shows 2D ELF views for two extreme cases of the interaction on the plane of the Au_7Kr cluster, *i.e.* at positions (a) and (d).

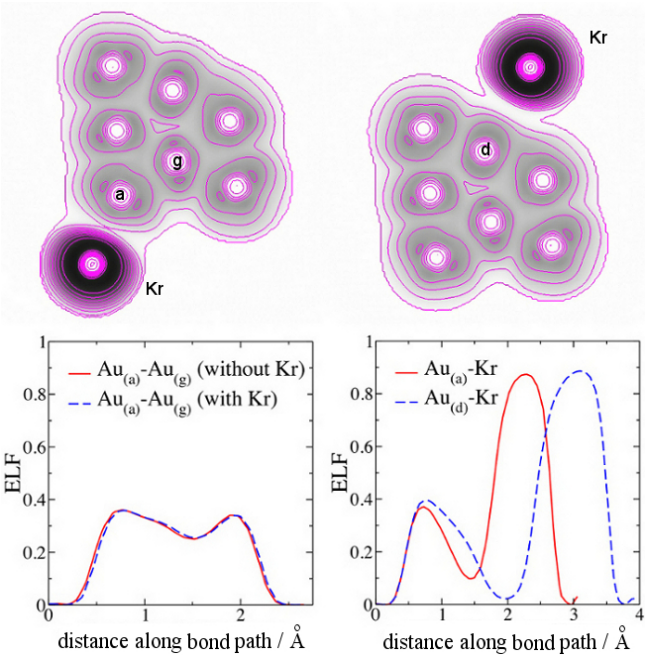

Figure 8: (**Above**) 2D electron localization function ELF for the Au_7Kr cluster for the two extreme cases of the interaction Au–Kr on the plane of the cluster. ELF is color-coded from zero (white) to one (black). (**Below left**) Profile of ELF along the interatomic region Au–Au between positions (a) and (g) for the bare cluster and for Au_7Kr when the krypton atom binds at (a). (**Below right**) Comparison of the profile of ELF along interatomic regions Au–Kr for the two cases shown in the upper part of this figure. Results obtained using PBE/GTH. Coordinate x is oriented along the bond path. Notation for atomic sites as for Fig. 6.

For the complete Au_7Kr system, we obtained ELF values in the range 0 to 0.9, and observe that there are saddle points of ELF in the Au–Au interatomic regions, which take values between 0.18 and 0.28 depending the pair of first neighbors observed. For the path shown in the lower-left part of Fig. 8 this value is ~ 0.25. It means that at this size, the gold cluster is still far to recover the metallic character of the bulk regime, since metallic bonds are defined for ELF~ 0.5. For the Au–Kr interaction at position (a) there is a saddle point of ELF=0.1 (see lower-right part of Fig. 8). ELF does not reveal the occurrence of a pure covalent bonding but reveals, however, the occurrence of orbital overlap. Notice that we are analyzing covalence in terms of the criteria established for ELF. For the case in which the krypton atom is around position (d), ELF along the Au–Kr path exhibits a region with values very close to zero. An analysis of the Laplacian of ELF in order to locate minima of the function along this region reveals a clear analytical discontinuity of ELF. At this site the electrostatic potential is weak and thus there is no significant effect from the spin density at this distance. Therefore, it is mainly a vdW interaction that maintains the krypton

atom bound in the vicinity of the cluster at this position. An estimation of the relative magnitude of the total Pauli repulsion can be made from the ELF value. The value of ELF for Kr binding at positions (a), (d) and (e), for a distance of 1.4 Å from the gold cluster (which is close to the reported atomic radius 1.35 Å [93]) are 0.10, 0.23 and 0.11, respectively. Therefore a smaller Pauli repulsion occurs at that distance when the Kr atom binds at (d) than when it binds at (a) or (e). The non-spherical ELF distribution around the krypton atom reveals an induced polarization due to the Au–Kr interaction. Polarization of the cluster accompanied by change transfer is observed in the case of binding at (a). Although no charge transfer occurs for binding at (d), distortion of ELF around the krypton atom show signs of change on its polarization.

Disentangling the combined effect of different types of interactions becomes more challenging the bigger and more asymmetric the cluster is, in part due to the lack of an explicit calculation of vdW energies. Thus we stop here our size progression and perform a complete trend analysis in the next section, introducing the effect of van der Waals interactions for the cluster sizes studied so far.

5 Overall trends and the role of the dispersion interactions

In this section we firstly show the overall trends of our results without including vdW interactions. Afterwards, we show general trends of our results including vdW corrections obtained using the two different schemes previously described in Section 3.3 (D3-BJ by Grimme [54,55] and TS by Tkatchenko-Scheffler [57]). Table 1 summarizes the uncorrected and dispersion corrected binding energies in terms of the binding length. This table also shows that for Au_7Kr and Au_9Kr clusters the dispersion interactions indeed affect some site preferences. For example in Au_7Kr, binding Kr atoms at typical vdW positions such as the higher coordinated site (b) or out of the plane (top) may occur with very close binding energies than at low coordinated sites such as (a), (e) or (c), even if the nature of the binding is different. Something similar occurs for Au_9Kr, where the higher coordinated site (d) or out of the plane (top) have similar binding energies than at the low coordinated site (a). This implies an interplay between dispersion and electrostatic contributions that leads to a degeneracy of the binding energy at (a) and (top) site. In this sense, our analysis of the binding for this cluster is compatible with the picture provided by Ghiringhelli *et al.* [35] about itinerary Kr atoms around the cluster.

The upper part of Fig. 9 shows the Au–Kr distances for the global minimum energy configurations of Au_nKr clusters obtained without including dispersion interactions. These distances increase from Au_2Kr to Au_6Kr, and we observe a monotonous behavior of the values between even and odd size clusters. The lower part of Fig. 9 shows the Au–Kr binding energies for the global minimum energy configurations of Au_nKr clusters obtained without including dispersion interactions in comparison to those obtained after including the dispersion corrections. The Kr binding energies do not vary uniformly as the cluster size increases and this behavior is preserved when including dispersion corrections. Also notice that the AuKr system behaves very differently to the clusters, therefore investigating the nature of the Kr bonding to the clusters by extrapolating the behavior of the AuKr system may lead to wrong conclusions. In particular, the larger Au–Kr distance and the smaller Kr binding energy in AuKr is presumably due to the less directional electrostatic interaction for AuKr contrary to the planar clusters. Presumably, the characteristics of Kr binding in AuKr would be closer to Kr binding for 3D high-symmetry clusters, with a spherical-like electrostatic potential.

Figure 10 shows the Kr binding energies as a function of the distance for a set of 27 global and local minima of all gold clusters studied here (as listed in Table 1) without including dispersion corrections. The shorter the bond length the lower the binding energy. In addition, this figure shows different types of fits including a term $\propto 1/r$ that corresponds to the electrostatic interaction

Table 1: Uncorrected and dispersion corrected Kr binding energies, for different binding sites at various cluster sizes. Uncorrected binding energies as obtained using PBE/GTH. r denotes the Au-Kr binding length. Binding sites follow the same notation as indicated in figures 2, 4 and 6. Data organized following the site preference given for each cluster by the uncorrected Kr binding energies E_b.

cluster size	site	r (Å)	E_b (meV)	E_b+$D3_{BJ}$ (meV)	E_b+TS (meV)
1		3.48	26	56	35
2	b	2.77	197	238	203
	top	4.28	12	44	40
3ob	c	2.87	120	162	128
	b	3.76	19	59	46
3ac	b	2.76	209	259	221
4	a	2.84	150	212	173
	b	3.58	24	59	41
5	b	3.08	67	114	81
	a	3.23	42	95	62
	c	3.81	19	74	61
6	a	3.12	60	106	74
	b	3.82	19	74	61
7	a	3.06	73	123	89
	e	3.11	62	122	87
	c	3.14	55	101	69
	f	3.19	45	91	60
	b	3.81	21	83	69
	d	3.92	17	70	59
	top	4.13	15	92	79
8	a	2.99	88	152	115
	b	4.17	19	80	73
9	a	3.08	65	114	81
	g	3.24	44	99	67
	f	3.24	42	109	73
	d	3.57	29	103	80
	top	4.16	15	98	82

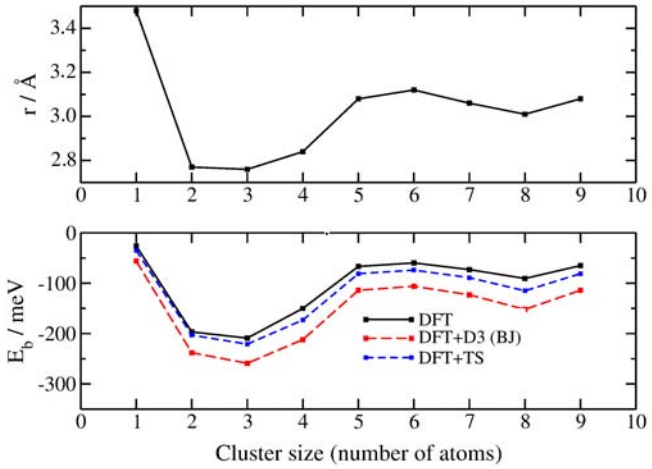

Figure 9: (**Above**) Au–Kr distances for the minimum energy configuration of Au_nKr clusters as obtained using PBE/GTH. (**Below**) Kr binding energies for the minimum energy configuration of Au_nKr clusters as obtained using PBE/GTH and in comparison with the corrected binding energies by using two different types of dispersion interactions.

and additional terms $\propto 1/r^a$ ($a = 6$ and $a = 12$) in order to provide insights on the type of interactions taking place. Notice that although the electrostatic potential is suitable to explain the Kr binding site preference in most cases, the binding energy as a function of the Au–Kr distance alone does not follow a mere $1/r$ behavior typical of the electrostatic interaction (see black curve in Fig. 10). In addition, since the electrostatic potentials are calculated from the undistorted clusters, they do not account for the effects of the deformation of the clusters after binding the Kr atom at each site. Drift from a perfect $1/r$ dependence on the Au–Kr distance originates from other type of interactions, such as Pauli repulsive forces, polarization, and Van der Waals-type forces.

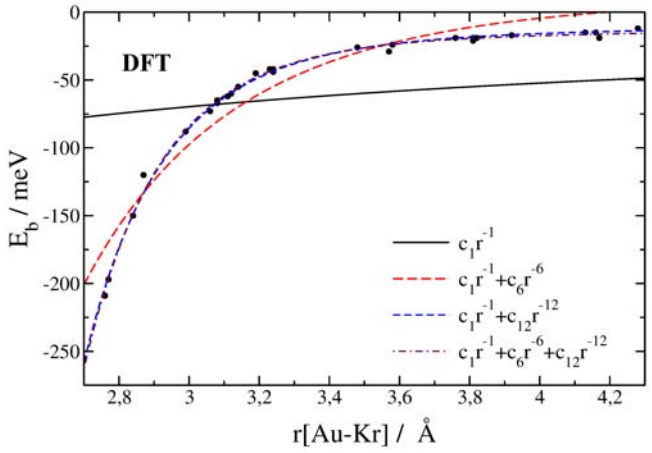

Figure 10: Kr binding energies (denoted by black dots) in terms of the Au–Kr distance for a set of 27 local and minimum energy configurations of the Au_nKr clusters studied here. Results obtained using PBE/GTH. The lines correspond to different types of fits of the original data. All fits include one term for the electrostatic interaction and three of them include additional terms for dispersion contributions. Parameters and asymptotic errors are reported in Table 2.

We perform different types of fits following a general form of the dispersion energy for the Au–Kr pair interaction:[57,78,80]

$$E_{disp} = -\sum_{a=6,8,10,\ldots} \frac{c_a}{r^a} \tag{5}$$

where r denotes the Au–Kr distance and c_a denotes a-order dispersion coefficients. No damping functions are considered in the fitting. We use $a = 6, 8, 10$, and 12 but in Fig. 10 we only report fits for $a = 6$ and $a = 12$, since the other two orders lead to intermediate cases. The contribution with the best fit and lower asymptotic standard error is an attractive potential in r^{-12}, while the term with the r^{-6} dependence shows a larger deviation (see Table 2). Note that a combination of r^{-1} and r^{-12} has a lower rms value (rms=3.6) in comparison to the combination of r^{-1} and r^{-6} (rms=15.0). Combination of the r^{-1}, r^{-6} and r^{-12} terms does not significantly improve the fit (rms=3.4) but the asymptotic standard errors increase tremendously, in particular for the r^{-6} term. Combination with other terms (r^{-8} or r^{-10}) does not improve the fit. What is interesting is the fact that despite the data being a mixture of open and closed shell clusters, all energy points are aligned on the r^{-12} curve, this implies that they all display the same kind of interaction. This is an unusual but not unlikely dependence and indicates that the DFT functional itself already accounts for short and medium-range dispersion interactions, since r^{-12} is of shorter range that r^{-6}. This is not necessarily contradictory to the different behaviour that we see for open vs closed shell clusters but it must mean that these differences are only valid for the preference to anchor at one position on the cluster but do not suggest a different nature of the dispersion interactions for even and odd size clusters.

It is worth noting that we observe a more scattered distribution when including dispersion. Upper part of Figure 11 shows the dispersion corrected binding energies using the D3(BJ) scheme proposed by Grimme. This scheme largely overcorrects the binding energies for short and medium ranges. Although a fit using the r^{-1} only leads to a small asymptotic standard error (about 7 %), looking at the rms values it is clear that a better approach to the real data distribution is given by including higher order contributions to the fit (see Table 2). In all fits the asymptotic standard error obtained for the r^{-12} contribution is lower than the one obtained for the r^{-6} contribution. Lower part of Figure 11 shows the dispersion corrected binding energies using the scheme proposed by Tkatchenko and Scheffler (TS). The fit obtained by including the r^{-1}, r^{-6} and r^{-12} contributions provides the smallest asymptotic standard errors together with the lowest rms value (see Table 2). In addition, the Au-Kr binding energies are not as overcorrected as with the D3-BJ scheme, *i.e.* both D3(BJ) and TS dispersion corrections schemes largely affect the Au-Kr binding energies for $r > 3.4$ Å, but the TS scheme does not largely affect those energies for short and medium ranges ($r < 3.4$ Å).

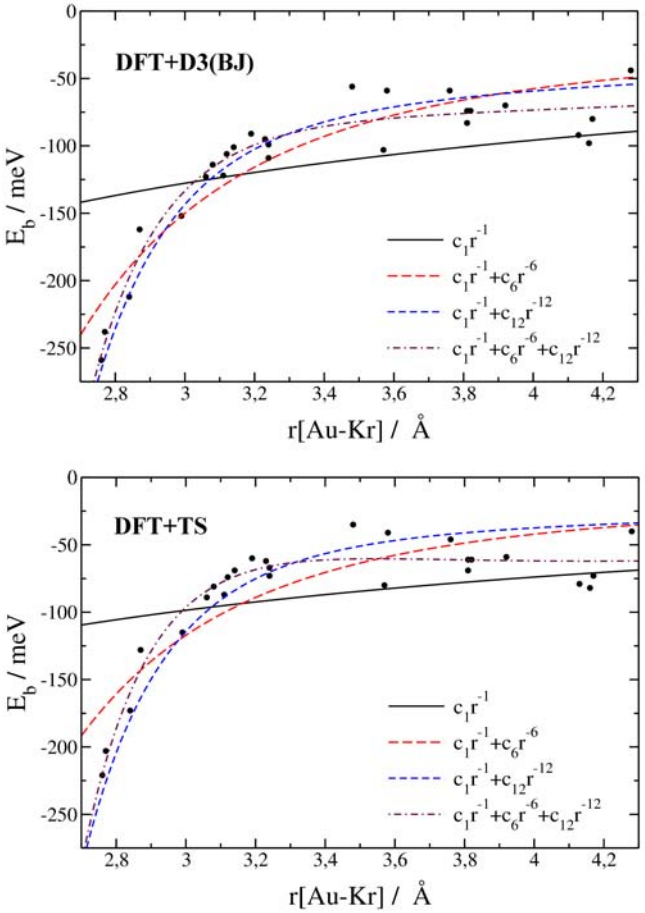

Figure 11: Kr binding energies (denoted by black dots) in terms of the Au–Kr distance for a set of 27 local and minimum energy configurations of the Au_nKr clusters studied here. (**Above**) Results obtained using PBE/GTH and dispersion corrected using Grimme's D3(BJ) scheme. (**Below**) Results obtained using PBE/GTH and dispersion corrected using Tkatchenko-Scheffler's TS scheme. The lines correspond to different types of fits of the original data. All fits include one term for the electrostatic interaction and three of them include additional terms for dispersion contributions. Parameters and asymptotic errors are reported in Table 2.

Table 2: Parameters obtained for each fit in figures 10 and 11. Values in parenthesis correspond to the asymptotic standard errors given in %. Right column shows the rms values for each fit. Smaller rms values denote a better fit.

c_1	c_6	c_{12}	rms
DFT (Fig. 10)			
−209.0 (14.4)	–	–	47.0
+67.6 (30.5)	−87525.8 (6.6)	–	15.0
−54.7 (6.0)	–	-3.6×10^7 (1.5)	3.6
−69.1 (11.6)	+9283.5 (51.2)	-3.9×10^7 (4.7)	3.4
DFT+$D3_{BJ}$ (Fig. 11)			
−383.2 (7.1)	–	–	42.2
−162.4 (19.5)	−69834.7 (12.7)	–	23.1
−228.8 (7.2)	–	-3.6×10^7 (7.6)	18.0
−330.1 (10.5)	+48944.5 (41.9)	-4.8×10^7 (16.6)	14.9
DFT+TS (Fig. 11)			
−295.7 (8.5)	–	–	39.0
−111.5 (31.8)	−58241.9 (17.0)	–	25.8
−141.3 (14.2)	–	-3.6×10^7 (9.3)	22.1
−321.5 (9.4)	+90497.8 (19.7)	-6.0×10^7 (11.5)	13.0

If we take the experimental value for AuKr binding energy, -30 ± 2 meV,[82] as a reference we see that the D3-BJ scheme largely overcorrects the theoretical binding energy from −26 meV to −56 meV (see Table 1). The TS correction also overcorrects the theoretical value but only up to −35 meV, which is still close to the experimental value. Notice that the TS-corrected binding energy for AuKr, 35 meV, closely agrees with the RCCSD(T) value reported by Plowright *et al.*[83] (36 meV). That would indicate that the TS correction is more suitable to be used for the description of this type of bonding in small gold clusters.

6 Conclusions

The study of noble gas-metal interaction is important to reveal the effect of the open-shell structure of the odd-numbered clusters, and the effect of the low dimensionality on the interatomic interactions. Some of these effects are translated into changes of vibrational frequencies, distortion of the structures, particular binding site preferences, changes in conductivity and changes in IR intensities due to polarization.

Noble gas-metal interactions in small gold clusters can be nearly but not accurately described by the features of the electrostatic potential. A more accurate model should include effect of repulsive Pauli forces and Van der Waals forces. These latest contributions start to be significant for Au_7Kr, Au_9Kr and possibly for other larger asymmetric clusters. In these cases, differences of vdW contributions to Kr binding at different sites are too large, and the site preference for Kr binding is indeed modified. Valuable information in order to understand the nature and role of the Au-Kr interatomic interactions in small gold clusters was obtained from reactivity analysis, electron localization function theory, and by including dispersion corrections.

Analysis of the frontier orbitals and of the ELF allows for a rationalization of the nature of the binding according to the site at which it occurs. From the ELF analysis we can extract qualitative changes on the dipole moment of the whole system. For example, that in the situation of a shorter bond length the charge transfer modifies the partial charge of both krypton atom and cluster, and that in the situation where a vdW-type interaction predominates, polarization occurs as a redistribution of charge in the krypton atom and in the cluster without charge transfer between them. The effects of the orbital overlap are modulated by the extension of the σ-type orbitals of both α-LUMO and β-LUMO. Charge transfer from the noble gas atom to the cluster as a consequence of this overlap modifies the charge distribution of the system. Even if in most cases partial charge exchange occurs, orbital overlap in Au–Kr binding is not strong enough to yield a covalent bond (understood in terms of ELF).

Although the different criteria to predict the site preference for Kr binding (e.g. reactivity indices, electro-

static potential, features of the LUMO) work relatively well for the various clusters studied here, for the Au_4 and Au_7 the site preference does not match the low-coordination criterion. In addition, for the open-shell clusters Fukui reactivity indices do not work in all cases, in particular for Au_7 and Au_9. This is presumably due to the fact that this indicator is based on the electrostatic charge only, so that it does not account for Pauli repulsion effects or for vdW dispersion interactions. Further exceptions to preferred binding at low-coordination sites or to sites predicted by the Fukui reactivity indices may be expected for larger clusters, in particular for large asymmetric clusters.

For the dispersion uncorrected binding energies, we could establish the order of a dispersion contribution ($\propto r^{-12}$), already included in the DFT functional, that rationalizes the deviation of the Kr binding energies from the pure electrostatic interaction. This indicates that regardless of the different choice of binding site for each individual cluster, the interaction is the same. That term is expected to account for short and medium-range dispersion interactions. By including dispersion corrections the corrected binding energies account for the long-range $\propto r^{-6}$ dispersion contributions, what is evidenced by fitting the binding energies using the combined effect of the r^{-1}, r^{-6} and r^{-12} contributions. Both dispersion correction schemes used overcorrect the binding energy of the AuKr system but the TS scheme keeps the corrected binding energy still close to the experimental value, which suggests that this is more suitable to describe the long-range dispersion interaction for Au-Kr binding in small gold clusters. Dispersion interactions modify the Kr binding site preference, in particular from Au_7 and Au_9, in which binding at vdW-type sites leads to binding energies of the same order that binding energies at low coordinated sites.

Acknowledgement This work was supported by a grant (SFB-569/TP-N1) from the German Science Foundation (DFG) through the Special Research Unit "Hierarchical Structure Formation and Function of Organic-Inorganic Nanosystems". We thank I. Ulusoy for helpful discussions and L. Leick for proofreading the manuscript.

References

(1) Silva, J. L. F. D.; Stampfl, C.; Scheffler, M. Xe adsorption on metal surfaces: First-principles investigations. *Phys. Rev. B* **2005**, *72*, 075424(1–19).

(2) Silva, J. L. F. D.; Stampfl, C. Trends in adsorption of noble gases He, Ne, Ar, Kr, and Xe on Pd(111)($\sqrt{3} \times \sqrt{3}$)R30°; All-electron density-functional calculations. *Phys. Rev. B* **2008**, *77*, 045401(1–13).

(3) Müller, J. E. Nature of the short-range interaction between noble gas atoms and metal surfaces. *Appl. Phys. A* **2007**, *87*, 433–434.

(4) Fernandez, E. M.; Soler, J. M.; Garzon, I. L.; Balbas, L. C. Trends in the structure and bonding of noble metal clusters. *Phys. Rev. B* **2004**, *70*, 165403(1–14).

(5) Li, X.-B.; Wang, H.-Y.; Yang, X.-D.; Zhu, Z.-H.; Tang, Y.-J. Size dependence of the structures and energetic and electronic properties of gold clusters. *J. Chem. Phys.* **2007**, *126*, 084505(1–8).

(6) Bonacic-Koutecky, V.; Burda, J.; Mitric, R.; Ge, M.; Zampella, G.; Fantucci, P. Density functional study of structural and electronic properties of bimetallic silver-gold clusters: comparison with pure gold and silver clusters. *J. Chem. Phys.* **2002**, *117*, 3120–3131.

(7) Häkkinen, H.; Landman, U. Gold clusters (Au_N, $2 \leq N \leq 10$) and their anions. *Phys. Rev. B* **2000**, *62*, R2287–R2290.

(8) Grönbeck, H.; Andreoni, W. Gold and platinum microclusters and their anions: comparison of structural and electronic properties. *Chem. Phys.* **2000**, *262*, 1–14.

(9) Bravo-Perez, G.; Garzon, I. L.; Novaro, O. Non-additive effects in small gold clusters. *Chem. Phys. Lett.* **1999**, *313*, 655–664.

(10) Hermann, A.; Krawczyk, R. P.; Lein, M.; Schwerdtfeger, P.; Hamilton, I. P.; Stewart, J. J. P. Convergence of the many-body expansion of interaction potentials: From van der Waals to covalent and metallic systems. *Phys. Rev. A* **2007**, *76*, 013202(1–10).

(11) Wesendrup, R.; Hunt, T.; Schwerdtfeger, P. Relativistic coupled cluster calculations for neutral and singly charged Au_3 clusters. *J. Chem. Phys.* **2000**, *112*, 9356–9362.

(12) Bravo-Perez, G.; Garzon, I. L.; Novaro, O. An initio study of small gold clusters. *J. Mol. Struct. Theochem* **1999**, *493*, 225–231.

(13) Hess, B. A.; Kaldor, U. Relativistic all-electron coupled-cluster calculations on Au_2 in the framework of the Douglas-Kroll transformation. *J. Chem. Phys.* **2000**, *112*, 1809–1813.

(14) Assadollahzadeh, B.; Schwerdtfeger, P. A systematic search for minimum structures of small gold clusters Au_n (n=2-20) and their electronic properties). *J. Chem. Phys.* **2009**, *131*, 064306(1–11).

(15) Han, Y.-K. Structure of Au_8: Planar or nonplanar? *J. Chem. Phys.* **2006**, *124*, 024316(1–3).

(16) Olson, R. M.; Varganov, S.; Gordon, M. S.; Metiu, H.; Chretien, S.; Piecuch, P.; Kowalski, K.; Kucharski, S. A.; Musial, M. Where Does the Planar-to-Nonplanar Turnover Occur in Small Gold Clusters? *J. Am. Chem. Soc.* **2005**, *127*, 1049–1052.

(17) Bauschlicher, C. W.; Langhoff, S. R.; Patridge, H. Theoretical study of the structures and electron affinities of the dimers and trimers of the group IB metals (Cu, Ag, and Au). *J. Chem. Phys.* **1989**, *91*, 2412–2419.

(18) Bauschlicher, C. W.; Langhoff, S. R.; Patridge, H. Theoretical study of the homonuclear tetramers and pentamers of the group IB metals (Cu, Ag, and Au). *J. Chem. Phys.* **1990**, *93*, 8133–8137.

(19) Das, K.; Balasubramanian, K. Spectroscopic properties of low-lying electronic states of Au_2. *J. of Mol. Spectrosc.* **1990**, *140*, 280–294.

(20) Balasubramanian, K.; Das, K. Excited electronic states of Au_3. *Chem. Phys. Lett.* **1991**, *186*, 577–582.

(21) Balasubramanian, K.; Feng, P. Y.; Liao, M. Z. Geometries and energy separations of 14 electronic states of Au_4. *J. Chem. Phys.* **1989**, *91*, 3561–3570.

(22) Liao, D.; Balasubramanian, K. Electronic structure of Cu_6, Ag_6, Au_6 and their positive ions. *J. Chem. Phys.* **1992**, *97*, 2548–2552.

(23) Seidel, S.; Seppelt, K. Xenon as a complex ligand: The tetra xenono gold(II) cation in $AuXe_4^{2+}(Sb_2F_{11}^-)_2$. *Science* **2000**, *290*, 117–118.

(24) Drews, T.; Seidel, S.; Seppelt, K. Gold-Xenon Complexes. *Angew. Chem. Int. Ed.* **2002**, *41*, 454–456.

(25) Hu, W.-P.; Huang, C.-H. The intrinsic stability of the noble gas-coordinated transition-metal complex ions. *J. Am. Chem. Soc.* **2001**, *123*, 2340–2343.

(26) Berski, S.; Latajka, Z.; Andres, J. The nature of the Au-Rg bond in the $[AuRg_4]^{2+}$ (Rg=Ar, Kr and Xe) molecules. *Chem. Phys. Lett.* **2002**, *356*, 483–489.

(27) Jamshidi, Z.; Far, M. F.; Maghari, A. Binding of Noble Metal Clusters with Rare Gas Atoms: Theoretical Investigation. *J. Phys. Chem. A* **2012**, *116*, 12510–12517.

(28) Ozin, G. A.; Mitchell, S. A.; McIntosh, D. F.; Mattar, S. M.; Garcia-Prieto, J. Novel copper-atom pairs in solid xenon. *J. Phys. Chem.* **1983**, *87*, 4666–4674.

(29) Ozin, G. A.; Baker, M. D.; Mitchell, S. A.; McIntosh, D. F. FT-FIR Spectroscopy of Ligand-Free Metal Clusters; Matrix Effects on the Molecular Geometry of Trichromium, Cr_3. *Angew. Chem. Int. Ed. Eng.* **1983**, *22*, 166–167.

(30) Fielicke, A.; Ratsch, C.; von Helden, G.; Meijer, G. The

far-infrared spectra of neutral and cationic niobium clusters: $Nb_5^{0/+}$ to $Nb_9^{0/+}$. *J. Chem. Phys.* **2007**, *127*, 234306(1–8).
(31) Knickelbein, M. B.; Menezes, W. J. C. Metal cluster-rare gas van der Waals complexes: Physisorption on a microscopic scale. *J. Phys. Chem.* **1992**, *96*, 6611–6616.
(32) Gehrke, R.; Gruene, P.; Fielicke, A.; Meijer, G.; Reuter, K. Nature of Ar bonding to small Co_n^+ clusters and its effect on the structure determination by far-infrared absorption spectroscopy. *J. Chem. Phys.* **2009**, *130*, 034306(1–11).
(33) Fielicke, A.; Rabin, I.; Meijer, G. Far-infrared spectroscopy of small neutral silver clusters. *J. Phys. Chem. A* **2006**, *110*, 8060–8063.
(34) Gruene, P.; Rayner, D. M.; Redlich, B.; van der Meer, A. F. G.; Lyon, J. T.; Meijer, G.; Fielicke, A. Structures of neutral Au_7, Au_{19} and Au_{20} clusters in the gas phase. *Science* **2008**, *321*, 674–676.
(35) Ghiringhelli, L. M.; Gruene, P.; Lyon, J. T.; Rayner, D. M.; Meijer, G.; Fielicke, A.; Scheffler, M. Not so loosely bound rare gas atoms: finite-temperature vibrational fingerprints of neutral gold-cluster complexes. *New J. Phys.* **2013**, *15*, 083003(1–22).
(36) Bader, R. F. W. *Atoms in Molecules. A Quantum Theory*; Oxford university press, 1994.
(37) Bader, R. F. W. A bond path: A universal indicator of bonded interactions. *J. Phys. Chem. A* **1998**, *102*, 7314–7323.
(38) Mendez, F.; Gazquez, J. L. Chemical reactivity of enolate ions: The local hard and soft acids and bases principle viewpoint. *J. Am. Chem. Soc.* **1994**, *116*, 9298–9301.
(39) Fukui, K. Role of frontier orbitals in chemical reactions. *Science* **1982**, *218*, 747–754.
(40) Fukui, K.; Yonezawa, T.; Shingu, H. A molecular theory of reactivity in aromatic hydrocarbons. *J. Chem. Phys.* **1952**, *20*, 722–725.
(41) Yang, W.; Parr, R. G. Hardness, softness, and the Fukui function in the electronic theory of metals and catalysis. *Proc. Natl. Acad. Sci. USA* **1985**, *82*, 6723–6726.
(42) Becke, A. D.; Edgecombe, K. E. A simple measure of electron localization in atomic and molecular systems. *J. Chem. Phys.* **1990**, *92*, 5397–5403.
(43) Silvi, B.; Savin, A. Classification of chemical bonds based on topological analysis of electron localization functions. *Nature* **1994**, *371*, 683–686.
(44) Kohout, M.; Savin, A. Atomic shell structure and electron numbers. *Int. J. Quantum Chem.* **1996**, *60*, 875–882.
(45) Kohout, M.; Savin, A. Influence of the core-valence separation of electron localization function. *J. Comput. Chem.* **1997**, *18*, 1431–1439.
(46) Silvestrelli, P. L. Van der Waals interactions in density functional theory using Wannier functions. *J. Phys. Chem. A* **2009**, *113*, 5224–5234.
(47) Mancera, L. A.; Benoit, D. M. Towards an understanding of the vibrational spectrum of the neutral Au7 cluster. *Phys. Chem. Chem. Phys.* **2013**, *15*, 1929–1943.
(48) CPMD Code, version 3.11.1. IBM Corp. and MPI Stuttgart, 2005; Car-Parrinello Molecular Dynamics.
(49) Perdew, J. P.; Burke, K.; Ernzerhof, M. Generalized gradient approximation made simple. *Phys. Rev. Lett.* **1996**, *77*, 3865–3868.
(50) Vanderbilt, D. Soft self-consistent pseudopotentials in a generalized eigenvalue formalism. *Phys. Rev. B* **1990**, *41*, 7892–7895.
(51) Goedecker, S.; Teter, M.; Hutter, J. Separable dual-space Gaussian pseudopotentials. *Phys. Rev. B* **1996**, *54*, 1703–1710.
(52) Hartwigsen, C.; Goedecker, S.; Hutter, J. Relativistic separable dual-space Gaussian pseudopotentials from H to Rn. *Phys. Rev. B* **1998**, *58*, 3641–3662.
(53) Krack, M. Pseudopotentials for H to Kr optimized for gradient-corrected exchange-correlation functionals. *Theor. Chem. Acc.* **2005**, *114*, 145–152.
(54) Grimme, S.; Antony, J.; Ehrlich, S.; Krieg, H. A consistent and accurate ab initio parametrization of density functional dispersion correction (DFT-D) for the 94 elements H-Pu. *J. Chem. Phys.* **2010**, *132*, 154104(1–19).
(55) Grimme, S.; Ehrlich, S.; Goerigk, L. Effect of the damping function in dispersion corrected density functional theory. *J. Comput. Chem.* **2011**, *32*, 1456–1465.
(56) Grimme, S.; Antony, J.; Ehrlich, S.; Krieg, H. DFT-D3 Package, version 3.1. Rev. 0. 2014; Implementation of DFT-D3.
(57) Tkatchenko, A.; Scheffler, M. Accurate Molecular Van Der Waals Interactions from Ground-State Electron Density and Free-Atom Reference Data. *Phys. Rev. Lett.* **2009**, *102*, 073005(1–4).
(58) Kresse, G.; Furthmüller, J. Efficient iterative schemes for *ab initio* total-energy calculations using a plane-wave basis set. *Phys. Rev. B* **1996**, *54*, 11169–11186.
(59) Billeter, S. R.; Curioni, A.; Andreoni, W. Efficient linear scaling geometry optimization and transition-state search for direct wavefunction optimization schemes in density functional theory using a plane-wave basis. *Comp. Mater. Sci.* **2003**, *27*, 437–445.
(60) Benoit, D. M.; Madebene, B.; Ulusoy, I.; Mancera, L. A.; Scribano, Y.; Chulkov, S. Towards a scalable and accurate quantum approach for describing vibrations of molecule-metal interfaces. *Beilstein J. Nanotechnol.* **2011**, *2*, 427–447.
(61) Mancera, L. A. Vibrational Anharmonicity in Small Neutral Gold and Silver Clusters. Ph.D. thesis, University of Ulm, Germany, 2010.
(62) Davidson, E. R. The iterative calculation of a few of the lowest eigenvalues and corresponding eigenvectors of large real-symmetric matrices. *J. Comput. Phys.* **1975**, *17*, 87–94.
(63) Filippone, F.; Parrinello, M. Vibrational analysis from linear response theory. *Chem. Phys. Lett.* **2001**, *345*, 179–182.
(64) Singh, U. C.; Kollman, P. A. An approach to computing electrostatic charges for molecules. *J. Comput. Chem.* **1984**, *5*, 129–145.
(65) Hockney, R. W. Potential calculation and some applications. *Meth. Comput. Phys.* **1970**, *9*, 136–211.
(66) Löwdin, P.-O. On the non-orthogonality problem connected with the use of atomic wave functions in the theory of molecules and crystals. *J. Chem. Phys.* **1950**, *18*, 365–375.
(67) Löwdin, P.-O. On the non-orthogonality problem. *Adv. Quantum Chem.* **1970**, *5*, 185–189.
(68) Schmidt, M. W.; Baldridge, K. K.; Boatz, J. A.; Elbert, S. T.; Gordon, M. S.; Jensen, J. H.; Koseki, S.; Matsunaga, N.; Nguyen, K. A.; Su, S. et al. General atomic and molecular electronic structure system. *J. Comput. Chem.* **1993**, *14*, 1347–1363, GAMESS code, version 11 (2008).
(69) Stevens, W. J.; Krauss, M.; Basch, H.; Jasien, P. G. Relativistic compact effective potentials and efficient, shared-exponent basis sets for the third-, fourth-, and fifth-row atoms. *Can. J. Chem.* **1992**, *70*, 612–630.
(70) Olson, R. M.; Gordon, M. S. Isomers of Au_8. *J. Chem. Phys.* **2007**, *126*, 214310(1–6).
(71) Njegic, B.; Gordon, M. S. Reaction mechanism of the direct gas phase synthesis of H_2O_2 catalyzed by Au_3. *J. Chem. Phys.* **2008**, *129*, 124705(1–6).
(72) Lee, T. J.; Jayatilaka, D. An open-shell restricted Hartree-Fock perturbation theory based on symmetric spin orbital. *Chem. Phys. Lett.* **1993**, *201*, 1–10.
(73) Lee, T. J.; Rendell, A. P.; Dyall, K. G.; Jayatilaka, D. Open-shell restricted Hartree-Fock perturbation theory: Some considerations and comparisons. *J. Chem. Phys.* **1994**, *100*, 7400–7409.
(74) Humphrey, W.; Dalke, A.; Schulten, K. VMD - Visual Molecular Dynamics. *J. Mol. Graphics* **1996**, *14*, 33–38.
(75) Kohout, M.; Wagner, F. R.; Grin, Y. Electron localization function for transition-metal compounds. *Theor. Chem. Acc.* **2002**, *108*, 150–156.
(76) Burdett, J. K.; McCormick, T. A. Electron localization in molecules and solids: the meaning of ELF. *J. Phys. Chem. A* **1998**, *102*, 6366–6372.
(77) Belpassi, L.; Tarantelli, F.; Sgamellotti, A.; Quiney, H. M. The electronic structure of alkali aurides. A four-component Dirac-Kohn-Sham study. *J. Phys. Chem. A* **2006**, *110*, 4543–4554.
(78) Grimme, S. Density functional theory with London dispersion corrections. *WIREs Comput. Mol. Sci.* **2011**, *1*, 211–228.
(79) Dobson, J. F.; White, A.; Rubio, A. Asymptotics of the Dispersion Interaction: Analytic Benchmarks for van der Waals Energy Functionals. *Phys. Rev. Lett.* **2006**, *96*, 073201(1–4).
(80) Stone, A. J. *The Theory of Intermolecular Forces*; Oxford University Press, 2002.
(81) Geethalakshmi, K. R.; Ruiperez, F.; Knecht, S.; Ugalde, J. M.; Morse, M. D.; Infante, I. An interpretation of the absorption and

emission spectra of the gold dimer using modern theoretical tools. *Phys. Chem. Chem. Phys.* **2012**, *14*, 8732–8741.
(82) Hopkins, W. S.; Woodham, A. P.; Plowright, R. J.; Wright, T. G.; Mackenzie, S. R. A velocity map imaging study of gold-rare gas complexes: Au-Ar, Au-Kr, and Au-Xe. *J. Chem. Phys.* **2010**, *132*, 214303(1–9).
(83) Plowright, R. J.; Watkins, M. J.; Gardner, A. M.; Wright, T. G.; Breckendridge, W. H.; Walliman, F.; Leutwyler, S. Electronic spectroscopy of the Au(6p)-Kr complex. *J. Chem. Phys.* **2008**, *129*, 154315(1–11).
(84) Ruamps, J. Production and study of the optical spectrum of diatomic metallic molecules and contribution to theoretical computation of intensities. *Ann. Physique (Paris)* **1959**, *13*, 1111–1157.
(85) Simard, B.; Hackett, P. High resolution study of the (0, 0) and (1, 1) bands of the $A0_u^+$-$X0_g^+$ system of Au_2. *J. Mol. Spectrosc.* **1990**, *142*, 310–318.
(86) Bishea, G.; Morse, M. Spectroscopic studies of jet-cooled AgAu and Au_2. *J. Chem. Phys.* **1991**, *95*, 5646–5659.
(87) Bondi, A. Vander Waals volumes and radii. *J. Phys. Chem.* **1964**, *68*, 441–451.
(88) Shen, Y.; BelBruno, J. J. Density functional theory study of the Jahn-Teller effect and spin-orbit coupling for copper and gold trimers. *J. Phys. Chem. A* **2005**, *109*, 512–519.
(89) Rusakov, A. A.; Rykova, E.; Scuseria, G. E.; Zaitsevskii, A. Importance of spin-orbit effects on the isomerism profile of Au_3: an *ab initio* study. *J. Chem. Phys.* **2007**, *127*, 164322(1–5).
(90) Howard, J.; Sutcliffe, R.; Mile, B. ESR spectrum of matrix isolated Au_3. *J. Chem. Soc. Chem. Commun.* **1983**, *23*, 1449–1450.
(91) Bishea, G. A.; Morse, M. D. Resonant two-photon ionization spectroscopy of jet-cooled Au_3. *J. Chem. Phys.* **1991**, *95*, 8779–8792.
(92) Guo, R.; Balasubramanian, K.; Wang, X.; Andrews, L. Infrared vibronic absorption spectrum and spin-orbit calculations of the upper spin-orbit component of the Au_3 ground state. *J. Chem. Phys.* **2002**, *117*, 1614–1620.
(93) Slater, J. C. Atomic radii in crystals. *J. Chem. Phys.* **1964**, *41*, 3199–3204.

Graphical TOC Entry